Mathematical and Computational Applications

MDPI

Article

Numerical Analysis of the Effect of the Vortex Finder on the Hydrocyclone's Split Water Ratio and Separation Performance

Vuyo T. Hashe and Thokozani J. Kunene *

Department of Mechanical Industrial Engineering Technology, University of Johannesburg, Doornfontein, Johannesburg 2028, South Africa; vhashe@uj.ac.za
* Correspondence: tkunene@uj.ac.za; Tel.: +27-11-559-6978

Abstract: Hydrocyclones are devices used in numerous areas of the chemical, food, and mineral industries to separate fine particles. A hydrocyclone with a diameter of *d*50 mm was modeled using the commercial Simcenter STAR-CCM+13 computational fluid dynamics (CFD) simulation package. The numerical methods confirmed the results of the different parameters, such as the properties of the volume fraction, based on CFD simulations. Reynolds Stress Model (RSM) and the combined technique of volume of fluid (VOF) and discrete element model (DEM) for water and air models were selected to evaluate semi-implicit pressure-linked equations and combine the momentum with continuity laws to obtain derivatives of the pressure. The targeted particle sizes were in a range of 8–100 microns for a dewatering application. The depth of the vortex finder was varied to 20 mm, 30 mm, and 35 mm to observe the effects of pressure drop and separation efficiency. The split water ratio increased toward a 50% split of overflow and underflow rates as the length of the vortex finder increased. It results in better particle separation when there is a high injection rate at the inlet. The tangential and axial velocities increased as the vortex finder length increased. As the depth of the vortex finder length increased, the time for particle re-entrainment into the underflow stream increased, and the separation efficiency improved.

Keywords: computational fluid dynamics; hydrocyclone; pressure drop; separation efficiency; split water ratio; vortex finder length

Citation: Hashe, V.T.; Kunene, T.J. Numerical Analysis of the Effect of the Vortex Finder on the Hydrocyclone's Split Water Ratio and Separation Performance. *Math. Comput. Appl.* **2023**, *28*, 50. https://doi.org/10.3390/mca28020050

Academic Editors: Hans Beushausen and Sebastian Skatulla

Received: 15 February 2023
Revised: 16 March 2023
Accepted: 20 March 2023
Published: 22 March 2023

1. Introduction

Hydrocyclones are used to sort solid particles or liquid droplets according to their size or density. The hydrocyclone is known as a dense medium cyclone (DMC). It is used for density-based separation rather than size-based separation [1]. In recent years, advances in computational technology have led to models based on fundamental fluid flow equations gaining center stage as tools for better understanding flow fields within the hydrocyclone and improving the design of this equipment. Computational fluid dynamics (CFD) is a powerful tool for studying the fluid dynamics of a wide range of physical systems, and it has been widely applied in engineering [2–4].

The pressure drop, split water ratio, and particle collecting efficiency are used to analyze the performance of hydrocyclones using computational fluid dynamics (CFD) [5]. Very recently, the main challenge for the hydrocyclones has been to minimize the pressure drop and maximize the separation efficiency to improve their performance. The split water ratio is defined as the ratio of the underflow volume flow rate to the overflow volume flow rate [6]. Other authors describe the split water ratio as the volume flow of the overflow to the volume flow of the inlet to effect the change in pressure drop via an inlet speed control [7,8]. The air-core dimension is key to predicting the split water to underflow, and a large air-core diameter leads to a condition known as "roping" [9]. The effects of the vortex finder diameter on the split water ratio and the short-circuit flow (measured by the difference between the feed flow rate and the low downward flow rate at the bottom of

the vortex finder) are crucial for particle separation. When the diameter is too small, the split water ratio (split water entrainment) is relatively high, indicating that the majority of particles, particularly fine particles, will circumvent the classification process and report to the underflow, which is not efficient [10]. Split water entrainment causes overgrinding of fine particles, excessive energy and water consumption, and product loss in particle categorization to support comminution circuits. These issues are compounded when excessive feed concentrations are used in order to enhance solids throughput. When there is no split water effect, which means that there is no entrainment of ultrafine particles into the underflow, then the classification system is efficient [11]. The split water ratio gradually becomes stable when the feed rate (velocity at the inlet) increases to a specific amount. High feed rates can often cause a substantial volume of fluid (water) to build in the underflow exit, causing a blockage of the discharge and interfering with the hydrocyclone's regular operation [12].

Hydrocyclones suffer from some unseparated particles that are usually grabbed by upward-moving fine particles and transferred into the internal rotating flow during downward particle movement, resulting in fine particle entrainment in the underflow (also referred to as short-circuit flow) [9,13]. This can have a significant impact on a hydrocyclone's separation precision. In general, the geometrical and operating parameters are the main factors that can be investigated to improve the separation precision of a hydrocyclone. An important feature to consider is the axial velocity in the hydrocyclone, which should prolong the retention time of particles in the hydrocyclone to improve the separation of particles [14,15].

The traditional approach to predicting a hydrocyclone's flow field and collection effectiveness is empirical. In the past decade, the application of CFD and relevant models for the numerical calculation of the gas flow field has grown more and more widespread. Kang et al. [16] applied the Reynolds stress model (RSM) that was developed by Anderson and Jakson [17] and combined the VOF model with the Lagrangian discrete phase model (DPM) to simulate the classification process of particles. It has been shown that the stochastic Lagrangian model can be used to follow the particle trajectories and assess the separation efficiency, and that the RSM model [18] can accurately represent the flow field in a gas cyclone. To determine the turbulent flow field within the 75 mm heavy dispersed phase particle separation cyclone, Rao & Zhao [19] used the RSM and volume of fluid (VOF) two-phase flow models. The kinematic properties and de-cementation process of weakly cemented particles happening in the internal flow field as well as the hydrocyclone effects were examined using the CFD and discrete element method (DEM) models by Fang et al. [20]. The DEM is a technique for creating parametric models to simulate and examine particle dynamics and is the best choice. Recently, Wang et al. [21] used unresolved CFD-DEM in coupling calculations of fluid flow fields, and particle dynamics are in time and space domains.

The flow dynamics inside such hydrocyclones are complicated. They involve intricate interactions between three different phases, such as gas-liquid, solid-solid, and liquid-solid [22,23]. Three numerical models VOF, DEM and a combination of VOF-DEM, were applied for each phase-type, respectively, in this study. A three-phase model was used in this study to investigate the effect of vortex finder length on the split water ratio in a hydrocyclone.

2. Numerical Method

2.1. Governing Equations

2.1.1. Transport Equation for Reynolds Stress Model (RSM)

The transport equation of the RSM model was originated by Anderson and Jakson [17]. This study presents the RSM model as it has been used to get a better fit for the flows in real separation processes. Yu et al. [24] proposed two different methods to track particles in multiphase flows, which have been adopted and presented in this paper. The anisotropic flow characteristic of the RSM model is owing to the highly turbulent fluid movement

inside the hydrocyclone. The RSM model has a grid void fraction ε_f. Its continuity equation and the momentum equation are:

$$\frac{\partial\left(\varepsilon_f\rho_f\right)}{\partial t}+\boldsymbol{u}\cdot\nabla\varepsilon_f\rho_f=0 \tag{1}$$

$$\frac{\partial}{\partial t}\left(\varepsilon_f\rho_f\boldsymbol{u}\right)+\nabla\cdot\left(\varepsilon_f\rho_f\boldsymbol{u}\boldsymbol{u}\right)=\varepsilon_f\left(-\nabla p+\nabla\cdot\left(\tau-\rho_f\boldsymbol{u}\boldsymbol{u}\right)+\rho g+\boldsymbol{f}_s\right)+\boldsymbol{f}_{pf} \tag{2}$$

where the fluid's density and velocity are indicated by ρ_f and $\boldsymbol{u}$, respectively. The definition of the viscous stress tensor τ is:

$$\tau=\mu\left((\nabla\boldsymbol{u})+\left(\nabla\boldsymbol{u}\right)^{\mathrm{T}}-\frac{2}{3}(\nabla\cdot\boldsymbol{u})\mathbf{I}\right) \tag{3}$$

where $\mathbf{I}$ and $\boldsymbol{\mu}$ stand for the identity tensor and fluid viscosity, respectively. The continuum surface force (CSF) model calculates the surface tension f_s of the liquid surface.

$$\boldsymbol{f}_s=\sigma\cdot\kappa\cdot\nabla\widetilde{\theta} \tag{4}$$

where σ is the surface tension coefficient, κ is the free-surface curvature, which is determined by using $\widetilde{\theta}$, an interpolation function of x (a separate point in space) to identify and describe various phase interfaces. The free-surface curvature κ, is calculated as:

$$\kappa=-\nabla\cdot\left(\nabla\widetilde{\theta}/\left|\nabla\widetilde{\theta}\right|\right) \tag{5}$$

The momentum exchange between the particle phase and fluid phase is where f_{pf} originates, and it is computed by:

$$\boldsymbol{f}_{pf}=\frac{1}{\Delta V}\sum_{i}^{n_p}\boldsymbol{F}_i^{pf}-\boldsymbol{F}_i^{\nabla p}-\boldsymbol{F}_i^{\nabla\cdot\tau}-\boldsymbol{F}_i^{\nabla(\rho uu)}-\boldsymbol{F}_i^{s} \tag{6}$$

where n_p is the number of particles and ΔV denotes the volume of the associated mesh cell.

The DEM-VOF model must take into account the interactions between particles and fluids, including drag force F_i^d, pressure gradient force $F_i^{\Delta p}$, viscous stress $F_i^{\nabla\cdot\tau}$, Reynolds stress $F_i^{\nabla(\rho uu)}$, capillary force F_i^s, virtual mass F_i^{vm}, Basset force F_i^B, Saffman lift F_i^{Saff} , and Magnus lift F_i^{Mag} . The drag force $\boldsymbol{F}_i^d$ is the force exerted by the fluid on solid particles with the relative velocity and is calculated by:

$$\boldsymbol{F}_i^d=\frac{\beta\mathrm{V}p}{1-\varepsilon_f}(\boldsymbol{u}-\boldsymbol{v}) \tag{7}$$

where $\boldsymbol{u}$ is the fluid velocity and ε_f is the local void fraction of the fluid. Between phases, the momentum exchange coefficient β is calculated by:

$$\begin{cases}\beta=150\frac{\left(1-\varepsilon_f\right)^2}{\varepsilon_f}\frac{\mu_g}{d_p^2}+1.75\left(1-\varepsilon_f\right)\frac{\rho_g}{d_p}\left|\boldsymbol{u}-v\right| & \varepsilon_f<0.8\\ \beta=\frac{3}{4}C_d\frac{\varepsilon_f\left(1-\varepsilon_f\right)}{d_p}\rho_f\left|\boldsymbol{u}-v\right|\varepsilon_f{}^{-2.65} & \varepsilon_f\geq 0.8\end{cases} \tag{8}$$

where d_p is the particle diameter and C_d is the sphere particle's drag coefficient, and given as:

$$C_d=\begin{cases}\frac{24}{\mathrm{Re}_p}\left(1+0.15\left(\mathrm{Re}_p\right)^{0.687}\right) & \mathrm{Re}_p<1000\\ 0.44 & \mathrm{Re}_p\geq 1000\end{cases} \tag{9}$$

The particle group's Reynolds number, Re_p is determined by:

$$\mathrm{Re}_p = \frac{\varepsilon_f \rho_f \left| \boldsymbol{u} - \boldsymbol{v} \right| d_p}{\mu_f} \tag{10}$$

Now, the total force $\boldsymbol{F}_i^{\mathrm{pf}}$ particle-fluid interaction is calculated by:

$$\boldsymbol{F}_i^{\mathrm{pf}} = \boldsymbol{F}_i^{d} + \boldsymbol{F}_i^{\nabla p} + \boldsymbol{F}_i^{\nabla \cdot \tau} + \boldsymbol{F}_i^{\nabla(\rho \boldsymbol{u} \boldsymbol{u})} + \boldsymbol{F}_i^{s} + \boldsymbol{F}_i^{vm} + \boldsymbol{F}_i^{B} + \boldsymbol{F}_i^{\mathrm{Saff}} + \boldsymbol{F}_i^{\mathrm{Mag}} \tag{11}$$

2.1.2. Discrete Element Model (DEM)

This paper uses a combined technique of the VOF and DEM with the RSM turbulence model to study liquid-gas-solid three-phase flows in hydrocyclones. This is because the VOF-DEM model captured the gas-liquid interface for particle flow. The approach of the selected models and their documentation are articulated in the STAR CD user guide [25].

The progress made in the past on major findings is mentioned by Zhu et al. [26], with an emphasis on the microdynamics, including packing/flow structure and particle–particle, particle–fluid, and particle–wall interaction forces. They conclude that for particle-scale research, discrete particle simulation is an excellent tool. This study adopted the VOF-DEM model as well. It modeled the interaction of the walls and the DEM particles with Hertz–Mindlin and the linear spring models, along with the physics. The interactions were particle-to-particle, particle-to-fluid, and particle-to-wall, as they played a major role in fluidization [26].

A particle can move in two different ways in granular multiphase flows: translation and rotation. Newton's second law could be used to explain these motions [27,28].

$$m_i \frac{dv_i}{dt} = \sum_j \boldsymbol{F}_{\mathrm{ij}}^{c} + \sum_k \boldsymbol{F}_{ik}^{nc} + \boldsymbol{F}_i^{f} + \boldsymbol{F}_i^{p} + \boldsymbol{F}_i^{g} \tag{12}$$

$$I_i \frac{d\omega_i}{dt} = \sum_j \left(\boldsymbol{M}_{ij}^{t} + \boldsymbol{M}_{ij}^{r} \right) \tag{13}$$

where v_i, ω_i, I_i, and m_i stand for a particle's translational, angular, mass, and moment of inertia, respectively. The i, j, and k subscripts denote the i, j, and kth particles, respectively. The forces of contact, noncontact, particle-fluid interaction, pressure gradient, and gravitational attraction are denoted as $\boldsymbol{F}_{\mathrm{ij}}^{c}, \boldsymbol{F}_{ik}^{nc}, \boldsymbol{F}_i^{f}, \boldsymbol{F}_i^{P}$, and $\boldsymbol{F}_i^{g}$, respectively. The tangential and rolling friction moments are denoted by the letters $\boldsymbol{M}_{ij}^{t}$ and $\boldsymbol{M}_{ij}^{r}$.

Calculating the contact force between particles is crucial for the DEM model. It is possible to separate the normal and tangential components of the contact force $\boldsymbol{F}_{\mathrm{ij}}^{c}$ [29,30].

$$\boldsymbol{F}_{\mathrm{ij}}^{c} = \boldsymbol{F}_{\mathrm{ij}}^{cn} + \boldsymbol{F}_{\mathrm{ij}}^{ct} \tag{14}$$

The expression for the normal component $\boldsymbol{F}_{\mathrm{ij}}^{cn}$ is:

$$\boldsymbol{F}_{\mathrm{ij}}^{cn} = -k_{ij}^{pp} \boldsymbol{\delta}_{n,ij} - \eta_{ij}^{pp} \boldsymbol{v}_{n,ij} \tag{15}$$

Where the definition of the tangential component $\boldsymbol{F}_{\mathrm{ij}}^{ct}$ is:

$$\boldsymbol{F}_{\mathrm{ij}}^{ct} = \begin{cases} -k_{ij}^{pp} \boldsymbol{\delta}_{t,ij} - \eta_{ij}^{pp} \boldsymbol{v}_{t,ij} & \left(\left| \boldsymbol{F}_{\mathrm{ij}}^{ct} \right| \le \mu^{pp} \left| \boldsymbol{F}_{\mathrm{ij}}^{cn} \right| \right) \\ -\mu^{pp} \left| \boldsymbol{F}_{\mathrm{ij}}^{cn} \right| \frac{v_{t,ij}}{\left| v_{t,ij} \right|} & \left(\left| \boldsymbol{F}_{\mathrm{ij}}^{ct} \right| > \mu^{pp} \left| \boldsymbol{F}_{\mathrm{ij}}^{cn} \right| \right) \end{cases} \tag{16}$$

where k, δ, η, and μ are, in turn, the spring constant, the particle overlap, the damping coefficient, and the friction coefficient. The superscripts n, t, and pp stand for normal, tangential, and particle-to-particle properties, respectively.

2.1.3. Volume of Fluid (VOF) Model

In order to represent the interface between two fluid phases, such as the gas–liquid and liquid–liquid interfaces, the phase volume fraction of each fluid phase is added to the VOF model. α_q is the qth phase's volume percent. By resolving the volume fraction of the qth phase's continuity equation, which is based on the fluid velocity, it is possible to track the interface in this model [31,32].

$$\frac{\partial \alpha_q}{\partial t} + \boldsymbol{u} \cdot \nabla \alpha_q = 0 \tag{17}$$

By adding the products of the density ρ_q and viscosity μ_q of each fluid phase and its associated volume fraction, the density and viscosity of the fluid are determined.

$$\rho = \sum_{q=1}^{n} \alpha_q \rho_q, \mu = \sum_{q=1}^{n} \alpha_q \mu_q \tag{18}$$

The volume of fluid model solves a single momentum equation across the entire field to determine the velocity that each phase shares.

$$\frac{\partial}{\partial t}(\rho \boldsymbol{u}) + \nabla \cdot (\rho \boldsymbol{u}\boldsymbol{u}) = -\nabla p + \nabla \cdot \left(\mu(\nabla \boldsymbol{u}) + \left(\nabla \boldsymbol{u}\right)^{\mathrm{T}}\right) + \rho g + \boldsymbol{f} \tag{19}$$

Surface tension f_s and fluid-particle interaction f_s are both contained in the variable f.

2.2. Solver

A higher degree of implicitness is achieved by considering the resistance coupling factors in the phase-bound SIMPLE algorithm and the coupled algorithm for the pressure-velocity coupling. A converged and temporary stable time step of 1.0×10^{-4} s was used in the simulations. The mixture of the two phases (liquid and gas) in the hydrocyclone was modeled using the properties in Table 1.

Table 1. Liquid and gas phases representing a two-phase fluid flow in the hydrocyclone.

Eulerian Phases	Material Properties		
	Density	Dynamic Viscocity	Molecual Weight
Water (Liquid phase)	997.561 kg/m^3	8.887×10^{-4} Pa-s	18.0153 kg/kmol
Air (Gas phase)	1.2 kg/m^3	1.85508×10^{-5} Pa-s	28.9664 kg/kmol

The polydisperse rubber microparticles had a size range of 8–100 microns, and their properties are indicated in Table 2. The spherical particles of ten divisions of diameter (8 µm to 100 µm) were modeled using the Rosin–Ralmmer distribution [33]. The distribution parameters are the mean diameter of 78 µm. The chosen Schiller-Naumann model exhibits a flattened solid concentration profile and an enhanced secondary flow. The interphase drag force between particles was also calculated in this multiphase flow investigation [34]. The inlet velocities were varied at 3, 5, and 10 m/s (Table 3) to investigate the separation and split-water ratio effects of vortex finders under these conditions.

Table 2. Polydisperse rubber microparticles properties.

Lagrangian Phase	Material Properties		
	Density	Poission's Ratio	Young's Modulus
Rubber	1100.0 kg/m^3	0.45	5.17×10^5 Pa

Table 3. Geometry and boundary conditions of hydrocyclone of base case.

Parameter	Boundary Type	Variable
Feed Rate (m/s)	Inlet velocity	3, 5, 10
Underflow Diameter (mm)	Pressure outlet (Pa)	0
Overflow Diameter (mm)	Pressure outlet (Pa)	0
Vortex finder Depth (mm)	Wall	20, 30, 35

2.3. Hydrocyclone Geometry and Mesh Generation

The geometry of the hydrocyclone that was used in this computational study is shown in Figure 1, and Table 3 indicates the varied parameters of the model. It is a conventional hydrocyclone for separating mineral particles with specific diameters (cone base d = 50 mm).

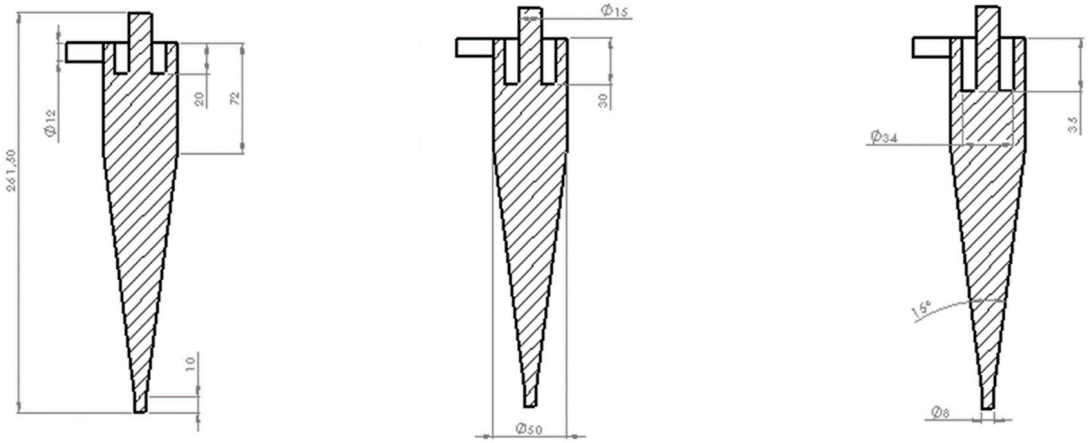

(**a**) (**b**) (**c**)

Figure 1. Geometry of hydrocyclone of base case of three vortex finder (VF) lengths, (**a**) 20 mm, (**b**) 30 mm and (**c**) 35 mm, respectively [15].

Figure 2a–d show that mesh grids were used to partition the domain entirely. For accurate numerical results, the quality and quantity of CFD meshes are crucial. In order to improve grid quality, the entire flow field of the hydrocyclone was discretized using polyhedral grids.

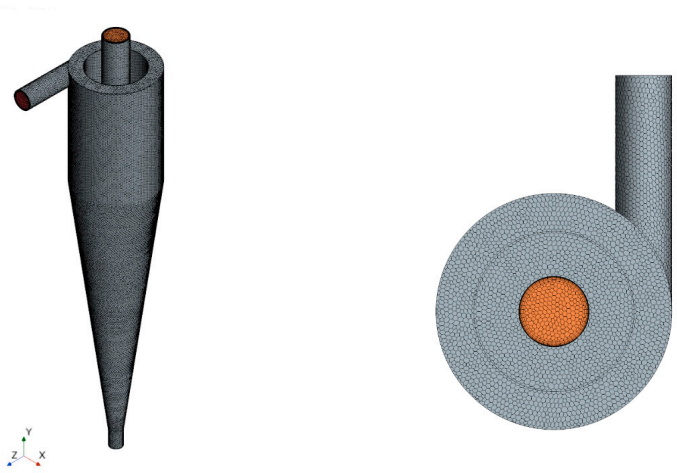

(**a**) (**b**)

Figure 2. *Cont.*

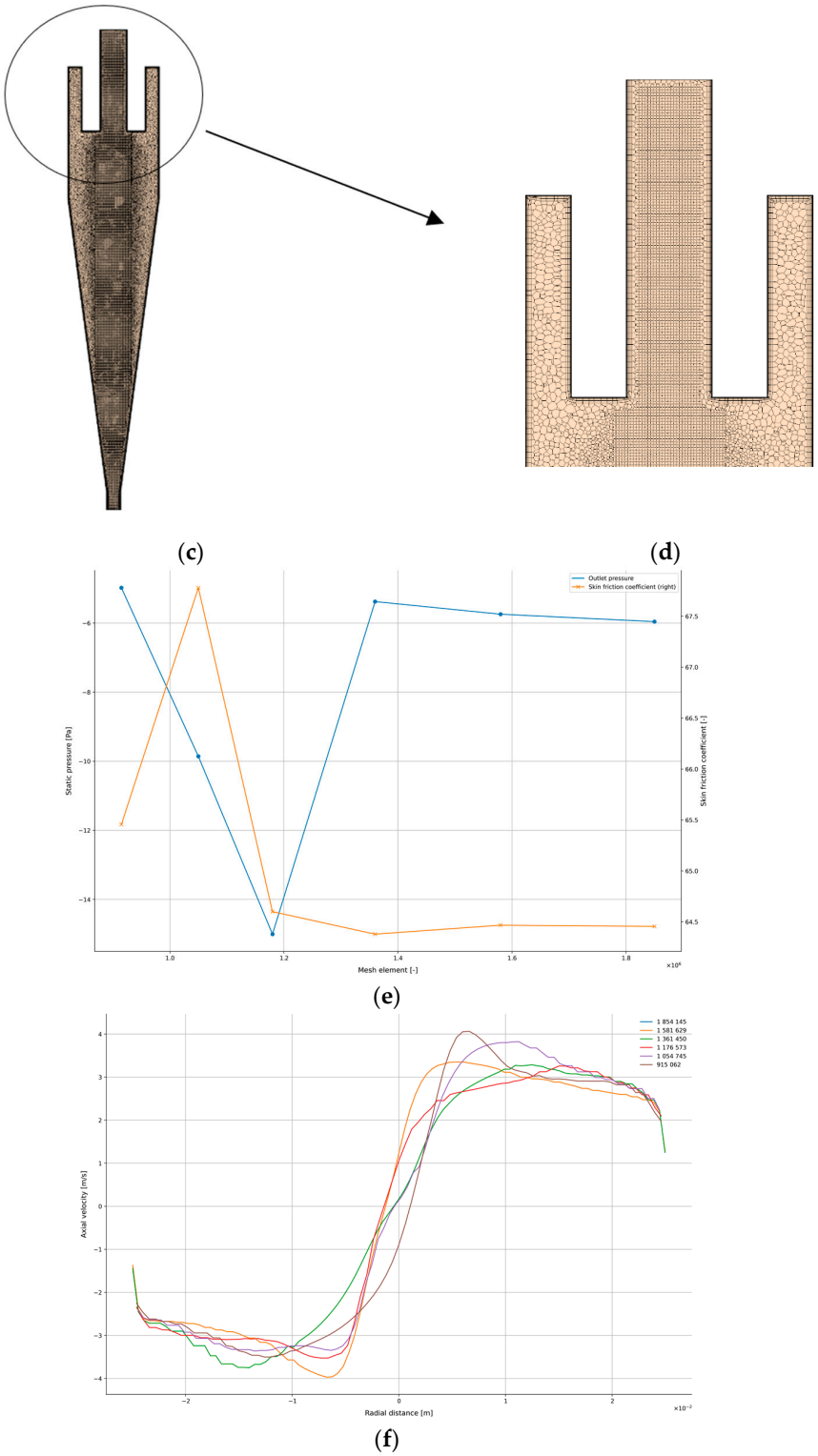

Figure 2. Polyhedral elements of the VF-20 mm model with (**a**) isometric and (**b**) top views, (**c**) plane view of the vortex finder diameter, (**d**) cut-away by the vortex finder length, mesh sensitivity study based on (**e**) outlet pressure at the overflow and wall skin friction coefficient; and (**f**) axial velocity profiles at radial distance within the entrance to the vortex finder, respectively.

Figure 2e,f show a grid-independent test that was conducted to find the optimum mesh density for this numerical study. A highly fine grid is computationally more expensive but is required to provide adequate mesh resolution. A convergence criterion for the simulations was established in two forms: grid changes based on output parameters of the

outlet pressure at the overflow and the wall skin friction coefficient. The remaining form was based on the axial velocity at the entrance of the vortex finder. These inform our study on the pressure difference that the overflow pressure would have on the premise that the variation of vortex finder length increases pressure drop and improves the separation of finer particles exiting at the overflow. Therefore, including the wall skin friction coefficient in the convergence criterion contributes well to the discussion of friction.

The axial velocity profiles in Figure 2f are the last addition to the convergence criterion. They were used to track the extrusion of air in the overflow. The axial velocity profiles demonstrated fewer changes near the air-core region (radial distances 0 and -0.001 m, within the cylindrical section of the hydrocyclone) in the sizes of the elements between 1.3615×10^6 and 1.8541×10^6. The air core shifted to the left in this region. Air is being extruded and is declining due to the changes between the forced vortex and the free vortex. However, as the element sizes increase, axial velocity profiles cluster well at the outer regions of the hydrocyclone diameter except for the courser elements of 9.1506×10^5 and 1.0547×10^6. This convergence occurs because of the elements that are between 1.3615×10^6 and 1.8541×10^6. Thus, further increasing the number of grids would have less effect on simulation accuracy. A grid size of 1.5815×10^6 elements was selected to produce the numerical results of this study.

2.4. Model Validation

The numerical method is validated by comparing the computed findings to those of tests on particle flow separation in hydrocyclones published in the literature. Dueck et al. [35] employed a two-fluid model to evaluate multiphase flow and hydrocyclone performance over a wide range of feed solids concentrations, giving special emphasis to the effects of vortex finder diameter, length, and feed rate. This literature was chosen since it used the same numerical methodology as the current study. In addition, the hydrocyclone measured $d50$ in size. For this investigation, we had to select a hydrocyclone with an injection velocity of 3 m/s as our goal. Overall, the trends found in the numerical conducted using the RSM with VOF-DEM model are in good agreement as the trends found the separation efficiency from literature are similar with the current study. The classification of particles from this study (Figure 3b) is noted to have the same "fish-hook" effect as shown in Figure 3a, which is from the literature.

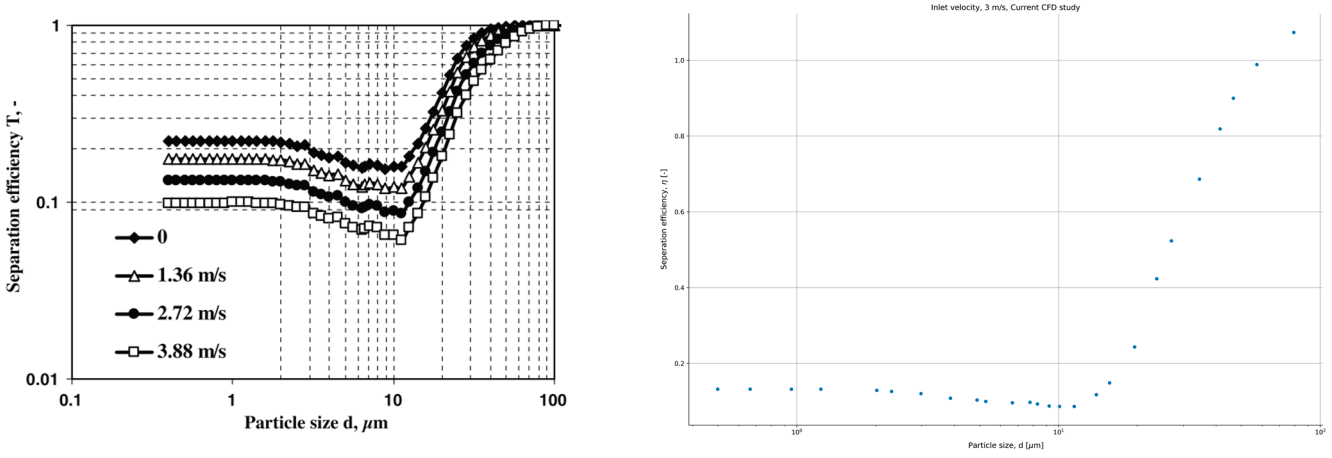

(**a**) (**b**)

Figure 3. Model validation against (**a**) Simulated partition curves of a 50-mm hydrocyclone curves for different injection velocities [35], Reproduced with permission from Dueck et al., Mechanism of hydrocyclone separation with water injection; published by Elsevier, 2010. (**b**) Current CFD for a 3 m/s inlet velocity.

3. Results

3.1. Effects of Water Volume Fraction Due to a Split Water Ratio

The water volume fraction contours predicted by the different models are shown in Figures 4–6. The water presence in the vortex finder component significantly influences the flow conditions, and it is important to implement this method so that the separation is not affected negatively. Thus, a desirable split water ratio is very important to obtain.

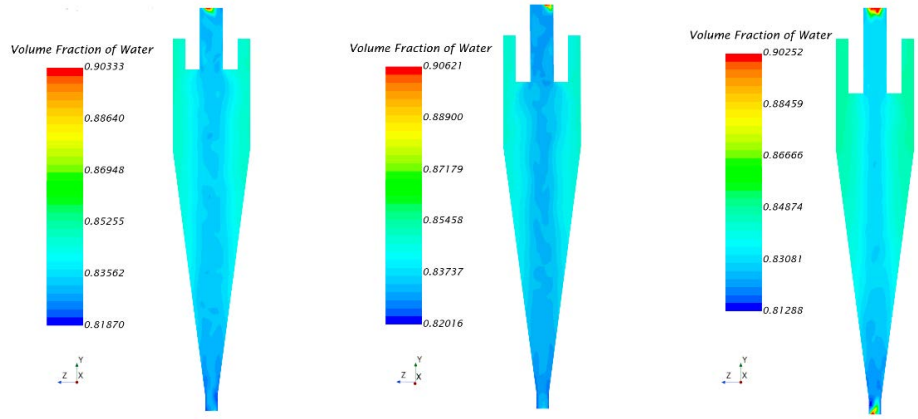

(**a**) (**b**) (**c**)

Figure 4. Volume fraction of water at 60 s at an inlet feed velocity of 3 m/s (**a**) VF = 20 mm (**b**) VF = 30 mm (**c**) VF = 35 mm.

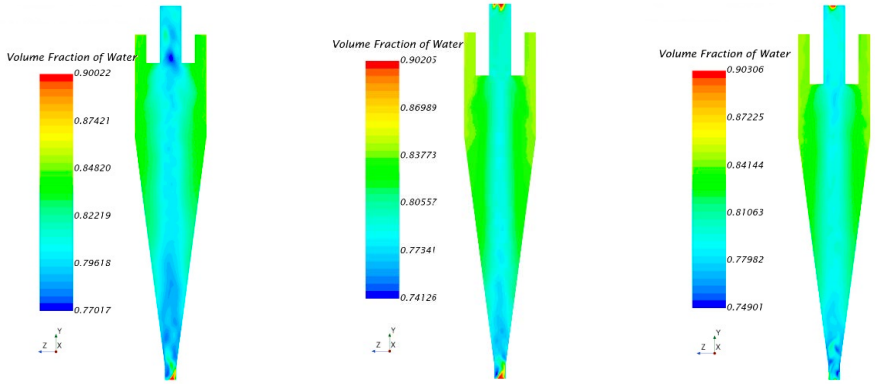

(**a**) (**b**) (**c**)

Figure 5. Volume fraction of water at 60 s at an inlet feed velocity of 5 m/s (**a**) VF = 20 mm (**b**) VF = 30 mm (**c**) VF = 35 mm.

Figure 4 depicts the progression of the water volume fraction (enhancement of the air column due to less water) formation process and the establishment of stability at various vortex finder lengths. The air column has a significant impact on the separation performance of the hydrocyclone, and its formation is an essential indicator of the flow field's stability in the hydrocyclone.

The feed velocity is maintained at 3 m/s, and the volume fraction of 0.9 is archived in the underflow and overflow at a VF of 35 mm (Figure 4c). It has balanced the water split and made fine particles classified enough to overflow. This study follows a definition of the split water ratio, the ratio of the volume flow of the overflow to the volume flow of the inlet, to effect the change in pressure drop via an inlet speed control. The longer vortex finder length (VF = 35 mm) provides a more significant pressure drop.

Figure 5a–c show an increased speed from 3 m/s to 5 m/s for the varying vortex finder lengths. It can be seen that there is more water at the overflow with VF = 30 mm and VF = 35 mm compared to VF = 20 mm. Only a higher amount of water with a volume

fraction of 0.903 in the overflow in the case of VF = 35 mm. With a higher inlet speed and a shorter vortex finder length, an excessively high rotating speed can coarsen the overflow particles. It can be explained that the flow field's turbulence and fluctuation are increased, which substantially disrupts the centrifugal settling of particles and discharges more water in the overflow, which would attract finer particles. In this case, VF = 35 mm with a feed rate velocity of 5 m/s draws finer particles to the overflow.

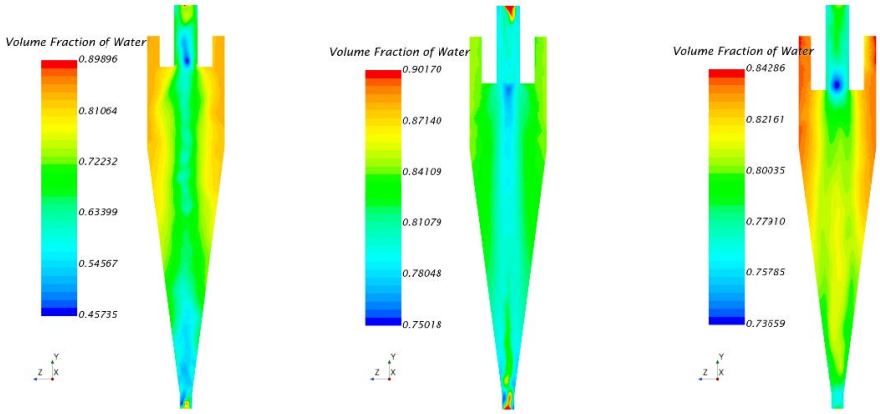

(**a**) (**b**) (**c**)

Figure 6. Volume fraction of water at 60 s at an inlet feed velocity of 10 m/s (**a**) VF = 20 mm (**b**) VF = 30 mm (**c**) VF = 35 mm.

A balanced presence of water fraction of around 90% (in the overflow and underflow regions in Figure 4c) is present across the vortex finders at a feed rate velocity of 3 m/s, which provides steady and stable separation. The mixture of various water qualities in the vortex finder region is pronounced, and undesirable short-circuiting is then expected at higher speeds where there is much water in the underflow, as seen for a 5 m/s feed with a VF of 20 and 30 mm (Figure 5a,b).

Figure 6a–c show an increased speed from 5 m/s to 10 m/s, simulating an excessive feed rate for the varying vortex finder lengths. In comparison, it means that more energy input is experienced. It can be seen that there is more water in the air core column, and it is unstable, which means there is poor separation. There is much volume fraction of water and disturbance from an air core in the conical section of the hydrocyclone. It can be explained that higher feed speeds result in more particles building up in the conical part's underflow zone, ultimately obstructing the overflow's outlet. It means the axial velocity in the inner vortex (air core column) increases, directing more water into this region.

In terms of particles in a compound hydrocyclone, the finer particles flow where there is more water. It is seen in Figure 6c that there is a large volume of water in the outer vortex in the cylindrical section. It suggests increased centrifugal forces are pushing the finer particles and more water outward. This situation would favor coarser-heavier particles inwardly but reduce the residence time of the particles in the hydrocyclone. They quickly discharge into the underflow as the axial velocity highly maneuvers them. It strongly suggests that higher feed rates are not desirable. The vortex finder length has too little influence at this point to cause much of an increase in the pressure drop and encourage better classification. Therefore, the control of the pressure drop in the hydroclyclone would be in the feed rate.

3.2. Effects of Pressure Drop to a Split Water Ratio

The distributions of pressure in the hydrocyclones for various vortex finder lengths and inlet feed velocities are shown in Figures 7–9. The distribution of pressure exhibits similar variations. The pressure-drop gradually increased from the wall surface to the center, reaching its peak around the air core before swiftly decreasing to the lowest point in

the air column. The primary driving force that encourages the flow of fine particles toward the center is the pressure gradient force caused by a pressure drop.

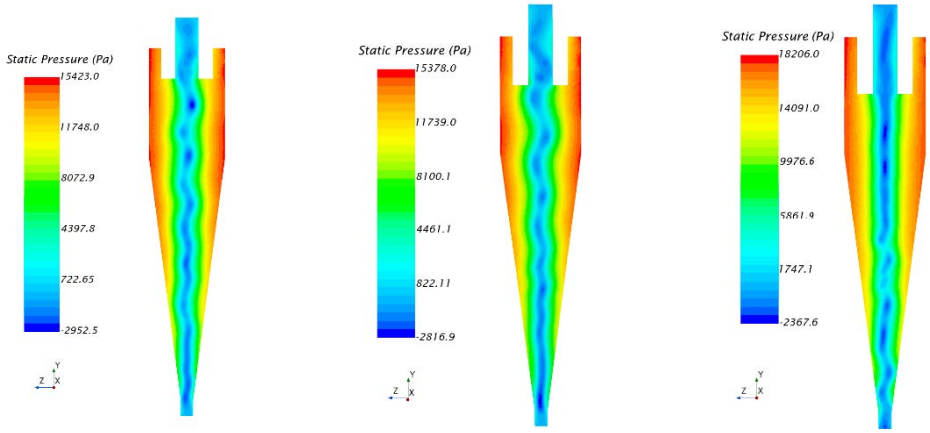

(**a**) (**b**) (**c**)

Figure 7. Static pressure at 60 s at an inlet feed velocity of 3 m/s (**a**) VF = 20 mm (**b**) VF = 30 mm (**c**) VF = 35 mm.

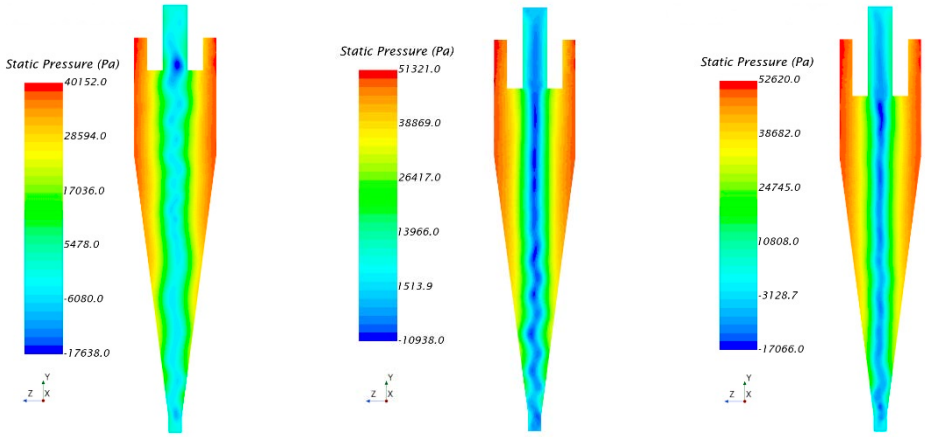

(**a**) (**b**) (**c**)

Figure 8. Static pressure at 60 s at an inlet feed velocity of 5 m/s (**a**) VF = 20 mm (**b**) VF = 30 mm (**c**) VF = 35 mm.

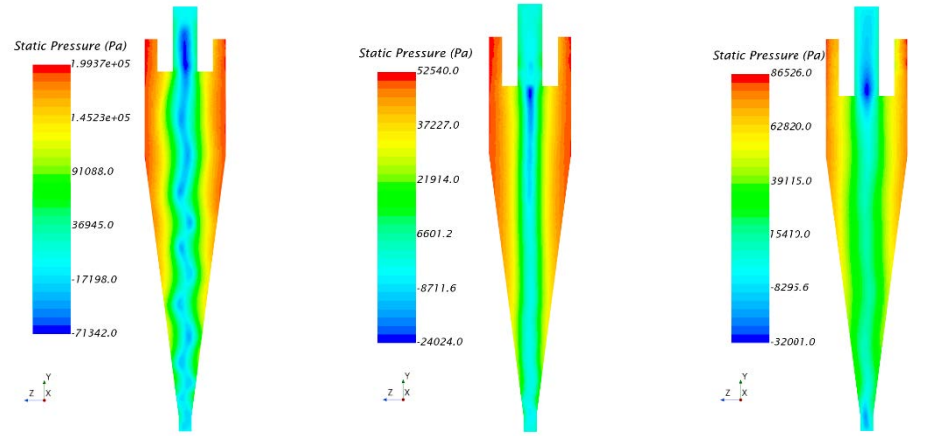

(**a**) (**b**) (**c**)

Figure 9. Static pressure at 60 s at an inlet feed velocity of 10 m/s (**a**) VF = 20 mm (**b**) VF = 30 mm (**c**) VF = 35 mm.

Figure 7a indicates that 3 m/s favors a moderate inflow of tangential velocity as the air core is stable, and it suggests a better classification of the particles at VF = 20 mm. The pressure drop is less than VF = 30 and 3VF = 35 mm. However, as shown in Figure 7c, as the vortex finder length increases, the 3 m/s inlet velocity lacks the necessary tangential velocity to form an intense pressure of −2367.6 Pa in the inner vortex. The air core is unstable around the conical region of the hydrocyclone. It can be explained that the vortex strength was reduced, and less energy was used due to the vortex finder length increasing, which lowered the tangential velocity. Moreover, the pressure-drop gradually increased as the vortex finder length grew longer.

Figure 8a shows that the air core in the VF = 20 mm is primarily reduced compared to the VF = 30 and 35 mm. The static pressure within this inner vortex, at 17,066 Pa in the VF = 35 mm, is shown in Figure 8c. The viscosity modification can explain the poor performance at VF = 20 mm. The tangential velocity directly affects the development of the air core. Thus, as the pressure drop is decreased, the air-core diameter decreases.

It is noticed that the good feed velocity should be 5 m/s as it provides a consistent decrease in suction pressure in the center of the hydrocyclone across the three vortex finder lengths. It forms a desirable air core to effect separation but might be very close to the spigot's diameter (underflow), which would cause a blockage if it grew further. It is not doing that at this instance, which is critically important for providing separation. The air core is not pronounced or consistent at higher feed speeds, as seen in Figures 8 and 9. An expectation is drawn in Figure 8b, where the velocity of 5 m/s makes better use of the friction length of the vortex finder (VF = 30 mm) and generates a suitable pressure drop to draw a suitable separation of the particles.

3.3. Effects of a Vortex Finder Length to a Split Water Ratio

An increase in the split water ratio increases separation efficiency only for fine particles; a drop in separation sharpness is seen in Figure 10. The overall partial separation efficiency improves as the feed rate is raised by increasing the pressure drop through the hydrocyclone for a shorter vortex finder length. However, to be energy efficient, a longer vortex finder can generate the necessary pressure drop and improve the separation efficiency. It has been discovered that increasing the underflow flow rate improves separation efficiency as a split water ratio of close to 50% is achieved at higher feed rates on longer vortex finder lengths. It means a balance of water is present at overflow and underflow to effect better separation of particles. This effect is because, even with the same split water ratio, the liquid flowing to the underflow carries heavier particles.

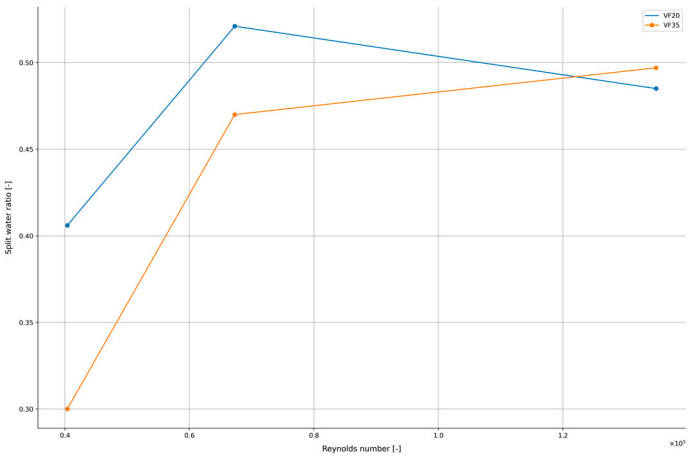

Figure 10. Progression of the split water ratio over the Reynolds number for two extreme cases.

4. Conclusions

This study used numerical simulation based on CFD to analyze the pressure drops, velocity feeds, volume percentage of water in the overflow and underflow, vortex finder

lengths, and split water ratio of three different hydrocyclone geometries. The key findings are discussed below.

With a longer vortex finder, the hydrocyclone's axial velocity was reduced, which increased particle separation by extending the period that particles were retained there. However, the split ratio decreased as the vortex finder length increased, which decreased the formation of secondary fluid. With an increase in feed rate velocity and a longer vortex finder length, the short-circuit flow rate was reduced, which significantly improved the hydrocyclone's separation accuracy.

Only for fine particles did an increase in the split ratio result in greater separation efficiency. The pressure decrease brought on by the vortex finder length between the spigot and the vortex finder region was quantified owing to this effort. Any modification to the hydrocyclone's operating and design parameters really alters the nature of the whirling flow patterns, which has an impact on the split water ratio and separation efficiency in the long run. It is important to split the feed within a hydrocyclone into the appropriate water volumetric ratios. If 50% of the feed went to the underflow, it would be meaningless to try to create a pure heavy liquid phase from a mixture of solids.

Author Contributions: Conceptualization, V.T.H.; methodology, V.T.H.; software, V.T.H. and T.J.K.; validation, T.J.K.; formal analysis, T.J.K.; investigation, T.J.K.; resources, V.T.H.; data curation, V.T.H.; writing—original draft preparation, V.T.H.; writing—review and editing, T.J.K.; visualization, V.T.H.; supervision, T.J.K.; project administration, V.T.H. All authors have read and agreed to the published version of the manuscript.

Funding: The APC was funded by the University of Johannesburg.

Acknowledgments: The author acknowledges the help from the Mechanical and Industrial Engineering Department of the University of Johannesburg. Special acknowledgement is due to the Center for High Performance Computing (CHPC) for the use of the cluster supercomputer called Lengau.

Conflicts of Interest: The authors declare no conflict of interest.

References

1. Bhamjee, M. Modelling of the Multiphase Interactions in a Hydrocyclone using Navier–Stokes and Lattice Boltzmann Based Computational Approaches. Ph.D. Thesis, University of Johannesburg, Johannesburg, South Africa, 2016.
2. Vieira, L.G.M.; Barrozo, M.A.S. Effect of vortex finder diameter on the performance of a novel hydrocyclone separator. *Miner. Eng.* **2014**, *57*, 50–56. [CrossRef]
3. Silva, N.K.G.; Silva, D.O.; Vieira, L.G.M.; Barrozo, M.A.S. Effects of underflow diameter and vortex finder length on the performance of a newly designed filtering hydrocyclone. *Powder Technol.* **2015**, *286*, 305–310. [CrossRef]
4. Padhi, M.; Mangadoddy, N.; Sreenivas, T.; Vakamalla, T.R.; Mainza, A.N. Study on multi-component particle behaviour in a hydrocyclone classifier using experimental and computational fluid dynamics techniques. *Sep. Purif. Technol.* **2019**, *229*, 115698. [CrossRef]
5. Durango-Cogollo, M.; Garcia-Bravo, J.; Newell, B.; Gonzalez-Mancera, A. CFD modeling of hydrocyclones-A study of efficiency of hydrodynamic reservoirs. *Fluids* **2020**, *5*, 118. [CrossRef]
6. Hwang, K.J.; Hsueh, W.S.; Nagase, Y. Mechanism of particle separation in small hydrocyclone. *Dry. Technol.* **2008**, *26*, 1002–1010. [CrossRef]
7. Jiang, J.; Ying, R.; Feng, J.; Wang, W. Computational and Experimental Study of the Effect of Operating Parameters on Classification Performance of Compound Hydrocyclone. *Math. Probl. Eng.* **2018**, *2018*, 7596490. [CrossRef]
8. Banerjee, C.; Climent, E.; Majumder, A.K. Mechanistic modelling of water partitioning behaviour in hydrocyclone. *Chem. Eng. Sci.* **2016**, *152*, 724–735. [CrossRef]
9. Delgadillo, J.A.; Rajamani, R.K. Exploration of hydrocyclone designs using computational fluid dynamics. *Int. J. Miner. Process.* **2007**, *84*, 252–261. [CrossRef]
10. Cui, B.; Zhang, C.; Wei, D.; Lu, S.; Feng, Y. Effects of feed size distribution on separation performance of hydrocyclones with different vortex finder diameters. *Powder Technol.* **2017**, *322*, 114–123. [CrossRef]
11. Galvin, K.P.; Iveson, S.M. New challenges for gravity concentration and classification of fine particles. *Miner. Eng.* **2022**, *190*, 107888. [CrossRef]
12. Zhang, Y.; Xu, M.; Duan, Y.; Yang, X.; Yang, J.; Tang, X. Influence of Feed Rate on the Performance of Hydrocyclone Flow Field. *Separations* **2022**, *9*, 349. [CrossRef]
13. Li, F.; Liu, P.; Yang, X.; Zhang, Y.; Li, X.; Jiang, L.; Wang, H.; Fu, W. Numerical analysis on the effect of the length of arc-shaped vortex finder on the hydrocyclone's flow field and separation performance. *Miner. Eng.* **2021**, *172*, 107172. [CrossRef]

14. Patra, G.; Chakraborty, S.; Meikap, B.C. Role of vortex finder depth on pressure drop and performance efficiency in a ribbed hydrocyclone. *S. Afr. J. Chem. Eng.* **2018**, *25*, 103–109. [CrossRef]
15. Mokonyama, L.; Kunene, T.J.; Tartibu, L.K. Numerical investigation of the hydrocyclone vortex finder depth on separation efficiency. In *MATEC Web of Conferences*; Skatulla, S., Ed.; EDP Sciences: Paris, France, 2021; Volume 347, p. 00039. [CrossRef]
16. Kang, S.G.; Kim, K.C.; Ryom, S.C.; Ri, J.H. Turbulence models and simulation method in the CFD simulation of 75-mm hydrocyclone. *Bilim. Madencilik Derg.* **2022**, *61*, 127–134. [CrossRef]
17. Anderson, T.B.; Jackson, R. Fluid Mechanical Description of Fluidized Beds. Equations of Motion. *Ind. Eng. Chem. Fundam.* **1967**, *6*, 527–539. [CrossRef]
18. Pandey, S.; Brar, L.S. On the performance of cyclone separators with different shapes of the conical section using CFD. *Powder Technol.* **2022**, *407*, 117629. [CrossRef]
19. Rao, G.; Zhao, H. Analysis of internal flow field performance of hydrocyclone based on CFD. *J. Phys. Conf. Ser.* **2022**, *2383*, 012027. [CrossRef]
20. Fang, X.; Wang, G.; Zhong, L.; Qiu, S.; Wang, D. A CFD–DEM analysis of the de-cementation behavior of weakly cemented gas hydrate–bearing sediments in a hydrocyclone separator. *Part. Sci. Technol.* **2022**, *40*, 812–823. [CrossRef]
21. Wang, M.; Liu, J.B.; Wang, X.F.; Yan, X.L.; Yao, L.M.; Yue, Q.B. Automatic determination of coupling time step and region in unresolved DEM-CFD. *Powder Technol.* **2022**, *400*, 117267. [CrossRef]
22. Artyukhov, A.E.; Sklabinskiy, V.I. Application of vortex three-phase separators for improving the reliability of pump and compressor stations of hydrocarbon processing plants. *IOP Conf. Ser. Mater. Sci. Eng.* **2017**, *233*, 012014. [CrossRef]
23. Lv, X.; Du, Y.; Du, S.; Xiang, L. Graded Preparation and Industrial Applications of Large-Ball Polyolefin Catalyst Carriers. *Catalysts* **2022**, *12*, 117. [CrossRef]
24. Yu, J.; Luo, X.; Wang, B.; Wu, S.; Wang, J. Analysis of Gas-Liquid-Solid Three-Phase Flows in Hydrocyclones through a Coupled Method of Volume of Fluid and Discrete Element Model. *J. Fluids Eng. Trans. ASME* **2021**, *143*, 111402. [CrossRef]
25. CD-ADAPCO. *STAR CCM+ User Guide (Version 4.02)*; CD-ADAPCO: New York, NY, USA, 2008.
26. Zhu, H.P.; Zhou, Z.Y.; Yang, R.Y.; Yu, A.B. Discrete particle simulation of particulate systems: A review of major applications and findings. *Chem. Eng. Sci.* **2008**, *63*, 5728–5770. [CrossRef]
27. Chen, F.; Jiang, S.; Xiong, H.; Yin, Z.; Chen, X. Micro pore analysis of suffusion in filter layer using tri-layer CFD–DEM model. *Comput. Geotech.* **2023**, *156*, 105303. [CrossRef]
28. Che, H.; Werner, D.; Seville, J.; Wheldon, T.K.; Windows-Yule, K. Evaluation of coarse-grained CFD-DEM models with the validation of PEPT measurements. *Particuology* **2023**, *82*, 48–63. [CrossRef]
29. Cheng, H.; Thornton, A.R.; Luding, S.; Hazel, A.L.; Weinhart, T. Concurrent multi-scale modeling of granular materials: Role of coarse-graining in FEM-DEM coupling. *Comput. Methods Appl. Mech. Eng.* **2023**, *403*, 115651. [CrossRef]
30. Li, S.; Duan, G.; Sakai, M. Development of a reduced-order model for large-scale Eulerian–Lagrangian simulations. *Adv. Powder Technol.* **2022**, *33*, 103632. [CrossRef]
31. Ganesan, S.; Tobiska, L. Finite Element Simulation of an Impinging Liquid Droplet. In *Micro-Macro-Interaction: In Structured Media and Particle Systems*; Bertram, A., Tomas, J., Eds.; Springer: Berlin/Heidelberg, Germany, 2008; pp. 173–185. [CrossRef]
32. Tiwari, S.; Kuhnert, J. A Numerical Scheme for Solving Incompressible and Low Mach Number Flows by the Finite Pointset Method. In *Meshfree Methods for Partial Differential Equations II*; Griebel, M., Schweitzer, M.A., Eds.; Springer: Berlin/Heidelberg, Germany, 2005; pp. 191–206.
33. Angelopoulos, P.M.; Peppas, A.; Taxiarchou, M. Modelling the Thermal Treatment and Expansion of Mineral Microspheres (Perlite) in Electric Furnace Through Computational Fluid Dynamics (CFD): Effect of Process Conditions and Feed Characteristics. *Miner. Process. Extr. Metall. Rev.* **2023**, 1–18. [CrossRef]
34. Liu, W.; He, Y.; Li, M.; Huang, C.; Liu, Y. Effect of drag models on hydrodynamic behaviors of slurry flows in horizontal pipes. *Phys. Fluids* **2022**, *34*, 103311. [CrossRef]
35. Dueck, J.; Pikushchak, E.; Minkov, L.; Farghaly, M.; Neesse, T. Mechanism of hydrocyclone separation with water injection. *Miner. Eng.* **2010**, *23*, 289–294. [CrossRef]